Effect of particle size, morphology, and hardness on cold gas dynamic sprayed aluminum alloy coatings

B. Jodoin [a,*], L. Ajdelsztajn [b], E. Sansoucy [a], A. Zúñiga [c], P. Richer [a], E.J. Lavernia [b]

[a] Department of Mechanical Engineering, University of Ottawa, Ontario, Canada K1N 6N5
[b] Department of Chemical Engineering and Materials Science, University of California, Davis, CA 95616, USA
[c] Departamento de Ingeniería Mecánica, Universidad de Chile, Santiago, Chile

Abstract

This work describes recent progress in Cold Gas Dynamic Spraying process of conventional and nanocrystalline 2618 (Al–Cu–Mg–Fe–Ni) aluminum alloy containing Sc. As-atomized and cryomilled 2618+Sc aluminum powders were sieved in two ranges of particle size (below 25 μm and between 25 and 38 μm), and sprayed onto aluminum substrates. The mechanical behavior of the powders and the coatings was studied using the nanoindentation technique, while the microstructure was analyzed using scanning and transmission electron microscopy. The influence of the powder microstructure, morphology and behavior during deposition on the coating properties was analyzed. It was concluded that the hard cryomilled particles do not experience extensive plastic deformation, and therefore failed to form a coating as dense as those produced using the gas-atomized spherical powder, despite the fact that the irregular shape cryomilled particles presented higher flight and impact velocities than the gas-atomized spherical particles. It was also observed that the influence of the particle morphology on the particle velocities is more pronounced for the larger particle size range (between 25 and 38 μm).

Keywords: Cold Gas Dynamic Spraying; Velocity measurement; Particle morphology; Nanocrystalline materials

1. Introduction

Cold Gas Dynamic Spraying (CGDS) represents recent development in the family of thermal spray processes. It was developed in the last decade based on experimental results revealing the possibility to produce dense coatings by accelerating micron-size feedstock powder beyond a material dependant critical velocity [1–3] and directing the particle flow towards the workpiece to be coated. Under this condition, it is foreseen that the particles impact the substrate and undergo intense plastic deformation that disrupts the thin film surfaces and results in intimate conformal contact under a very high localized pressure, thus creating a coating [4]. In order to achieve the required particle impact velocity, the feedstock powder particles are injected in a supersonic gas flow that ensures the proper gas/particle momentum transfer. This flow is generated using a DeLaval nozzle and inert gases such as helium or nitrogen are generally used as the propellant gas due to their aerodynamic properties [4]. The main feature that distinguishes CGDS from other thermal spray processes is the fact that particle heating is reduced to such extent that in-flight melting and/or softening is prevented, although theoretical models indicate that localized melting is possible under adiabatic sheer instability conditions during impact [5]. Consequently, CGDS is considered to be a solid-state process. This process particularly combined with the fact that the feedstock powder particles are only exposed to inert gases makes it attractive for the production of oxide free and nanocrystalline coatings.

Nanocrystalline materials are characterized by a microstructural length scale in the 1–100 nm range [6]. A large fraction of the atoms in these materials are associated with grain boundaries or interfacial boundaries when the grain size is small enough [7]. Thus, a significant amount of interfacial components between neighboring atoms associated with grain boundaries contributes to the exceptional physical properties

* Corresponding author. Tel.: +1 613 562 5800x6280; fax: +1 613 562 5177.
E-mail address: jodoin@genie.uottawa.ca (B. Jodoin).

of nanocrystalline materials [7]. Mechanical alloying/milling techniques have been used extensively to produce nanocrystalline feedstock powder [8–10]. These techniques use a high-energy ball milling process, in which elemental or pre-alloyed powders are used to produce materials with controlled microstructures. During mechanical milling, welding and fracturing of particles result in severe plastic deformation. The grain refinement process due to severe plastic deformation can be divided into three stages; starting with the localization of deformation into shear bands with high dislocation density, which is followed by annihilation and recombination of dislocations, forming nanometer-scale sub-grains. This sub-grain structure extends throughout the sample during continued milling. The final stage is the transformation of the sub-grain boundary structure to randomly oriented high-angle grain boundaries [11]. The continuous process produces micron-size agglomerates with a nanocrystalline structure. A special type of milling, also used to produce nanocrystalline powder is the cryogenic milling process, often referred to as cryomilling. During cryomilling, liquid nitrogen is continuously introduced to the milling process creating a slurry. This process was first described in the literature for Al–Al_2O_3 composites [12,13]. The advantages of cryogenic milling include [11,13–16]: reduced oxygen contamination from the atmosphere; larger convective heat transfer between the particles and the cryogenic media, which results in a lower particle temperature that favors fracturing over welding of ductile materials during the milling process; reduced milling time to achieve nanosize grains (hindering of microstructural recovery due to low temperature); and higher thermal stability of the material due to the presence of oxy-nitride dispersoids.

Studies have reported that the nanocrystalline structure of the initial feedstock powder produced by cryomilling is retained in coatings produced by the CGDS process. In particular, nanocrystalline aluminum [17] and nickel [18] alloy coatings have been successfully produced by CGDS. Despite these early successes in depositing these materials into dense nanocrystalline coatings, there is still a need to assess the general effects of cryogenic milling on the ability of the powder to be sprayed onto dense coatings when used in conjunction with the CGDS process. Consequently, the objective of the present work is to determine the effect of cryogenic milling on the ability of aluminum 2618 alloy to be sprayed when using the CGDS process. The 2618 aluminum alloy was selected in this study due to the ever increasing demand to manufacture weight efficient structures that are damage tolerant and that can operate at elevated temperatures. As such, the 2618 alloy has been developed and successfully used for intermediate temperature application, with the most famous application in the fuselage of the supersonic civil transportation vehicle Concorde [19]. The interest of combining cryomilled 2618 alloy powder and the CGDS process lies in the possibility of producing coatings that would retain the non-equilibrium microstructure features of the feedstock powder. In particular, the effect of the feedstock particle morphology and hardness induced by the cryogenic milling process are studied by comparing the particle impact velocity measured by laser diagnostic, the coating microstructure and hardness produced using cryomilled (nanocrystalline) and conventional powder with the same size range. Furthermore, a study of the effect of the particle size on the particle impact velocity and the coating microstructure is also performed for both (cryomilled and conventional) feedstock powders.

2. Experimental procedure

2.1. Powder preparation

The 2618 aluminum alloy powder (Al–Cu–Mg–Fe–Ni) with 0.16 wt.% Sc was produced by gas atomization using nitrogen as the inert atmosphere as well as the atomizing gas. The atomization temperature and dynamic pressure were set at 840 °C and 1360 kPa, respectively. The chemical composition of the atomized powder is presented in Table 1. The as-atomized powder was also mechanically milled at the rate of 180 rpm in a modified Union Process 01-ST attritor for 8 h under a liquid nitrogen environment, which was continuously supplied during milling to ensure complete immersion of the powders. Stainless steel balls with a 6.4 mm diameter were used as the grinding media and a ball-to-powder weight ratio of 32:1 was used. Details of the cryomilling system are described elsewhere [11]. Finally, after atomization and cryomilling, the powders were sieved to less than 25 μm and between 25 and 38 μm using 500 mesh and 400 mesh sieves (ASTM E-11) [20].

2.2. Coating preparation

The as-atomized and as-cryomilled powders were sprayed onto grit blasted (20 mesh grit) Al 6061 substrates using the CGDS coating system developed at the University of Ottawa Cold Spray Laboratory. The computerized system consists of a high-pressure gas control system, a commercial powder feeder (Praxair 1264 powder feeder, Praxair, Concord, NH, USA), a spray gun and a spraying chamber sealed off, providing the possibility of recycling the powder that has not adhered to the substrate. The gun is a converging–diverging nozzle allowing the particles to reach the high velocities required in the process. The system incorporates two sensors that measure the temperature and pressure at the nozzle inlet. A series of pressure sensors are also positioned along the nozzle length allowing monitoring of the pressure distribution and thus the propellant gas velocity in the nozzle while spraying. For this study, the substrate holder was equipped with a single-axis travel displacement system. The stagnation pressure and temperature were respectively set at 1.7 MPa and 20 °C and helium was used as propellant gas. The coatings were obtained by moving the substrate at a constant velocity of 8 mm/s in front of the jet exiting the spraying gun. The spraying standoff distance used was set at 20 mm and a single passage of the

Table 1
Chemical composition of the aluminum alloy powder (wt.%)

Cu	Mg	Fe	Ni	Si	Sc	Al
2.3	1.47	1.08	1.0	0.19	0.16	Bal

substrate in front of the gun was used to build-up the coatings on the substrate.

2.3. Particle velocity measurements

Particle velocities were measured with a commercial laser in-flight diagnostic system commonly used in thermal spray particle diagnostic, a DPV-CPS (Tecnar Automation Ltd., St-Bruno, Québec, Canada). While a continuous laser (laser diode power of 3 W) illuminates an interrogation volume (of approximately 4 mm radius), a dual-slit photomask captures the signal generated by individual particles passing in front of the sensor. The signal from the photosensor is amplified, filtered and analyzed. In-flight diagnostic of each individual particle that crosses the interrogation volume is performed by determining the time between the two peaks of the particle signal. Particle velocities are then obtained by dividing the distance between the two-slits by their time of flight. In this study, the velocity measurements were taken at a point 10 mm from the spraying gun exit. Furthermore, no substrate was positioned in front of the spraying gun since the resulting coating build-up would quickly mask the interrogation region.

2.4. Powder and coating characterization

The powder morphology and the coating microstructure were examined using a Philips XL30 FEG scanning electron microscope (SEM). Prior to SEM observations, the coating samples were sectioned from a transverse section and prepared by standard metallographic techniques. Secondary electron and backscattered electron images were obtained, and energy dispersive spectrometry (EDS) analyses were conducted on the coating samples. The microstructure of the coatings was also analyzed by transmission electron microscopy using a Philips CM 12 microscope operated at 100 kV. The samples were prepared by jet polishing using a mixture of 70% methanol and 30% nitric acid kept at −30 °C.

In order to investigate the mechanical properties of the powders and coatings nanoindentation studies were conducted in a MTS Nanoindenter® XP (Berkovich indenter) on the cross-section of the powders and the sprayed coatings. Powder samples were prepared for nanoindentation by mixing the cryomilled powder with a conductive molding compound. The samples were then ground (1200 grit) and polished (6, 3, 1, 0.25 μm diamond slurry). The same polishing procedures were used to prepare the cross-section of the sprayed coatings. The continuous stiffness measurement (CSM) approach was used to determine the hardness values from the nanoindentation tests [21]. An indentation depth of 500 nm was chosen in this study.

3. Results and discussion

3.1. Powder characterization

The as-atomized and as-cryomilled powder morphology is shown in Fig. 1. The as-atomized powder morphology is spherical, in agreement with what is typically seen in gas-atomized powder (Fig. 1A); on the other hand, cryomilling of the gas-atomized spherical powder led to the formation of irregular agglomerates, as shown in Fig. 1B. This morphology is attributed to the continuous welding and fracturing of the powder particles during the cryogenic mechanical milling process [11].

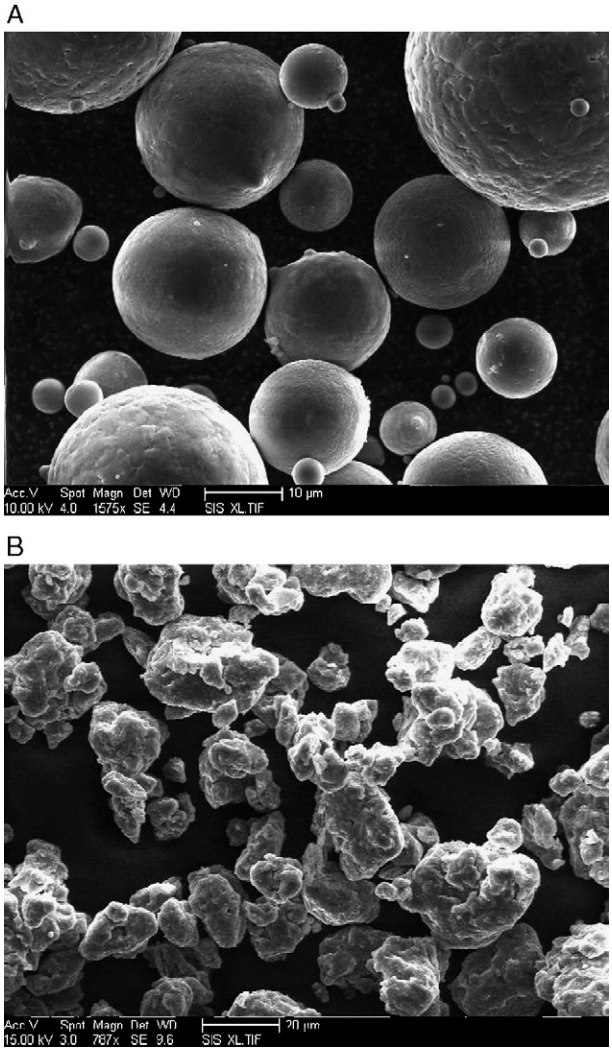

Fig. 1. Morphology of the powder: A) as-atomized, B) as-cryomilled.

The microstructural TEM evidence of the as-cryomilled powder can be found in detail elsewhere [22], and it consists of equiaxed, nanometric aluminum grains of approximately 50 nm, along with some slightly larger elongated grains. The presence of small Al_9FeNi particles that were broken down during the cryomilling process was also detected.

3.2. Velocity measurements

The particle velocity measurements were made using two different powder morphologies, as-atomized and as-cryomilled and two different powder ranges for each powder morphology, below 25 μm and between 25 and 38 μm. The velocity measurement quality will not be affected by the particle volumes and morphologies as long as the incoming laser radiation illuminating the particles is reflected such that it can be detected by the photosensor head [23]. It was found during the present study that when using the same powder mass flow rate for both powder size

ranges and morphologies, comparable particle flow rates were detected by the photosensor, thus confirming the ability of the diagnostic system to monitor the particle velocities independently of their sizes and morphologies. All the measurements were made in an interrogation volume located 10 mm downstream of the spray gun exit. This location is the closest location to the spray gun exit that can be accessed by the diagnostic system that ensures proper particle illumination by the laser. Locations closer to the gun exit exhibited too much reflection of the laser beam on the nozzle and resulted in improper particle illumination.

Even without the presence of a substrate located in front of the supersonic jet during the measurements, it is expected that the particle velocities measured in the interrogation region are representative of the particle impact velocities. In the presence of a substrate, the particles would go through a detached bow shock wave that is always present in front of the substrate to allow the supersonic flow reaching subsonic velocities and subsequently reaching the stagnation conditions on the substrate [24]. It has been shown that the abrupt change in the flow conditions brought about by this shock wave can affect the particles velocity depending on their mass densities and sizes. However, the particles used in this work will not experience a noticeable deceleration after the shock wave due to their size and the limited shock wave strength of the flow for this spray gun configuration [24]. Consequently, the measured particle velocities can be taken as the particle impact velocities. The velocity measurement results are summarized and presented in Table 2.

Table 2 reveals that for both size ranges the as-cryomilled powders reach higher average velocities than the as-atomized powder. As illustrated in Fig. 1, the cryomilling process generates non-spherical particles. From the aerodynamics perspective, this is beneficial to the powder acceleration as the drag coefficient of non-spherical particles is larger than the drag coefficient of spherical particles [25]. Since the drag force acting on a particle (D) is proportional to the particle drag coefficient (C_D), an increased drag coefficient leads to an increased drag force acting on the particle and thus to a higher particle velocity. This is expressed in Eq. (1), where ρ is the propellant gas mass density, V_{rel} is the relative velocity between the propellant gas and the particle and A_P is the particle projected surface area.

$$D = \frac{1}{2}\rho V_{rel}^2 A_P C_D \tag{1}$$

While the friction drag for spherical and non-spherical particles is likely to be similar, the shape form drag of the non-spherical particles will be higher leading to a higher total drag coefficient. This is attributed to the early boundary layer separation experienced by the irregular shaped particles as a result of the negative pressure gradient present on the particle surface for these shapes. As a result, a larger drag force will be applied to the non-spherical particles, promoting higher particle velocity at the end of the acceleration zone of the nozzle, as measured. Consequently, the morphology of the cryomilled powder makes it more suitable for the CGDS technology when solely looking at the achievable impact velocities.

Table 2
Average particle velocity measured for two different powder morphologies and two different powder size ranges (d=particle diameter)

Powder morphology and size range	Measured velocity (m/s)
As-atomized, d<25 μm	747±120
As-cryomilled, d<25 μm	790±150
As-atomized, 25 μm<d<38 μm	641±98
As-cryomilled, 25 μm<d<38 μm	716±132

It is worth noticing that the average particle velocity increase experienced by the larger size range of as-cryomilled particles compared to as-atomized particles (716 m/s compared to 641 m/s) is more important than the particle velocity increase experienced by the smaller size-range as-cryomilled particles compared to as-atomized particles (790 m/s compared to 747 m/s). This observation suggests that the increased acceleration experienced by the larger cryomilled particles is more substantial than for the smaller size-range cryomilled particles. Using Eq. (1) and Newton's law of motion the acceleration experienced by a particle can be expressed by Eq. (2), where dV/dt is the particle acceleration, V_p is the particle volume and ρ_p is the particle mass density.

$$\frac{dV}{dt} = \frac{\frac{1}{2}\rho V_{rel}^2 A_p C_D}{V_p \rho_p} \tag{2}$$

It is envisioned that two factors are causing the increased acceleration of the larger cryomilled particles. While both size ranges of cryomilled particles exhibit an increase in the drag coefficient, resulting in larger drag force acting on the particles as deduced from Eq. (1), it is possible that the larger cryomilled particles have a rougher surface and more irregular shape than the smaller cryomilled particles, contributing to a larger drag coefficient and consequently a larger drag force acting on the particle. Close observation of Fig. 1B tends to confirm that the larger particles have a more irregular shape than the smaller ones. Furthermore, it is possible that the effect of the increased drag coefficient is more pronounced for the large size range as the projected area–particle volume ratio (A_p/V_p) of the bigger particles is larger. This combination drag coefficient/projected area–particle volume ratio acts favorably and contributes to the larger velocity increase of the larger cryomilled particles, as deduced from Eq. (2). For the same aerodynamics considerations, the as-cryomilled particles would experience a larger deceleration force after the detached bow shock wave than the as-atomized if the shock strength was large enough to have an effect on the particles.

It can also be observed by looking at the results of Table 2 that for both the as-atomized and as-cryomilled powders, the smaller particle size range exhibits a higher average particle velocity. This is attributed to the fact that the gas/particle momentum transfer or particle acceleration imparted by the gas is proportional to $1/d$, based on Newton's law and assuming a spherical particle, where d is the diameter of the particle to be accelerated. Consequently, higher acceleration and, therefore, particle impact velocity are to be expected when using a powder with a smaller particle size distribution, as long as the jet Mach number is limited to values below or close to 3 [24]. It is

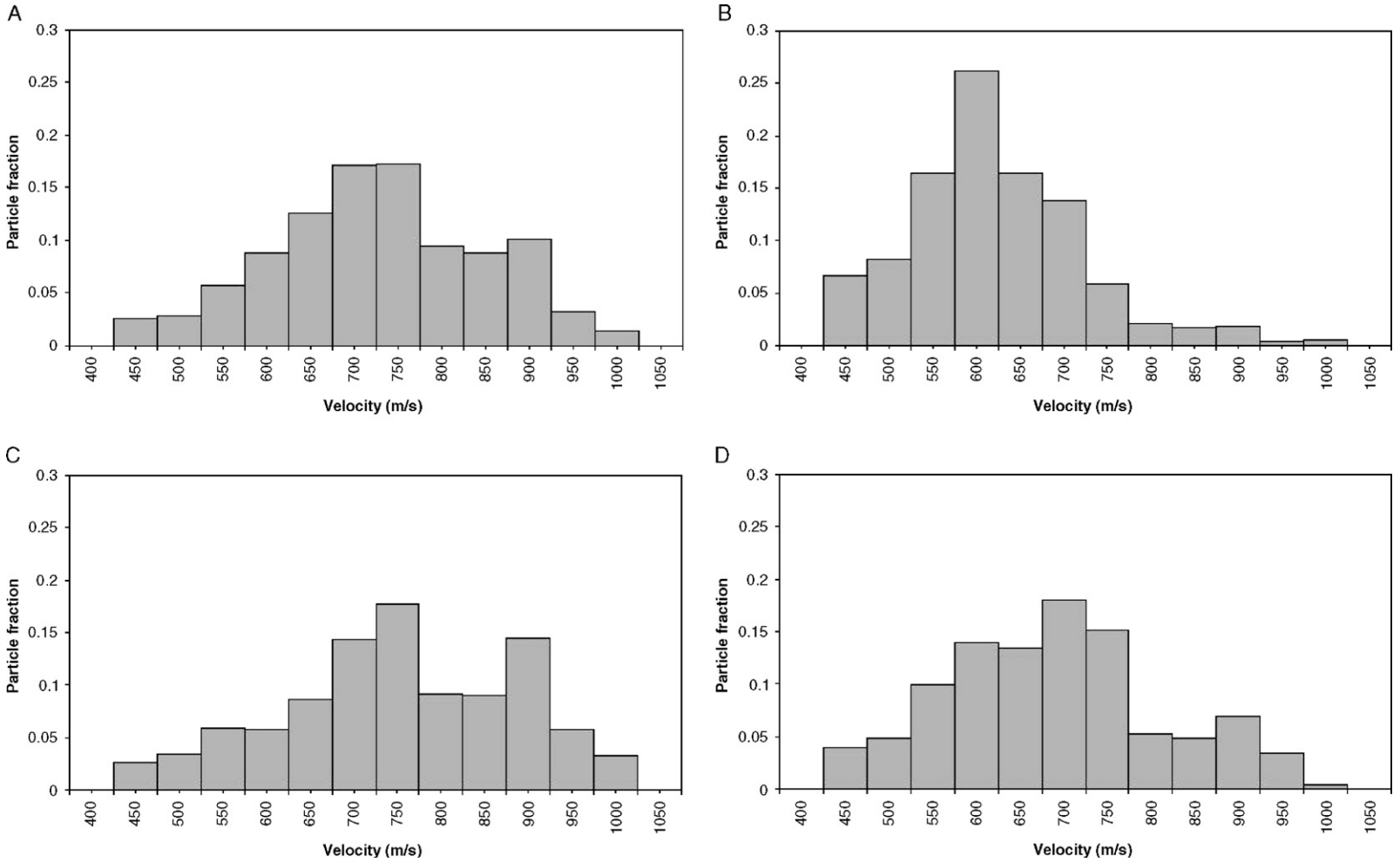

Fig. 2. Histograms of the particle velocity distribution as measured: (A) spherical (as-atomized) particles, $d<25$ μm, (B) spherical (as-atomized) particles, 25 μm$<d<$38 μm, (C) non-spherical (as-cryomilled) particles, $d<25$ μm, (D) non-spherical (as-cryomilled) particles, 25 μm$<d<$38 μm.

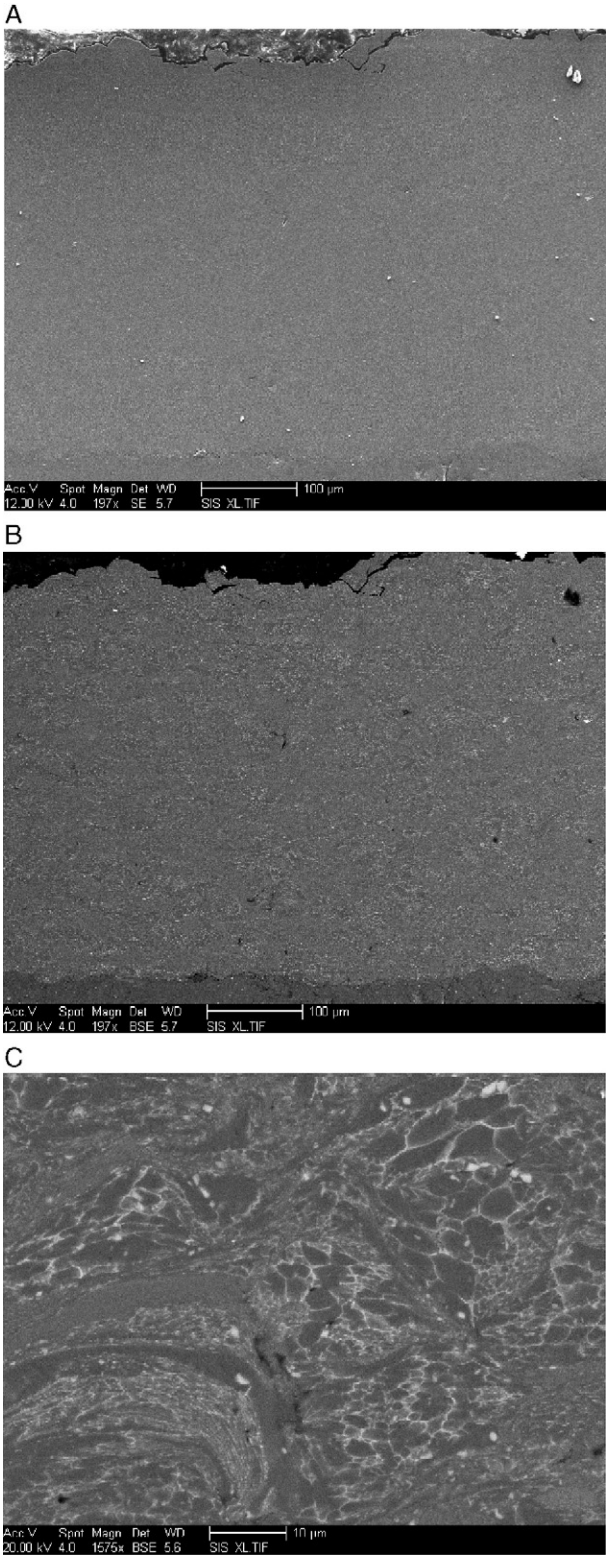

Fig. 3. Coatings produced by CGDS from as-atomized powder.

foreseen that a finer particle size distribution is more suitable for the CGDS process.

Fig. 2 presents the histograms of the particle velocity distribution, as measured with the laser diagnostic system for the four cases studied. As can be observed from Fig. 2(A) and (C), the morphology change induced by cryomilling does not affect the nature of the particle velocity distribution for the smaller range of particles ($d<25$ µm); it only causes a slight shift towards a higher velocity. A similar conclusion can be applied to the size range 25 µm$<d<$38 µm as observed from Fig. 2(B) and (D)

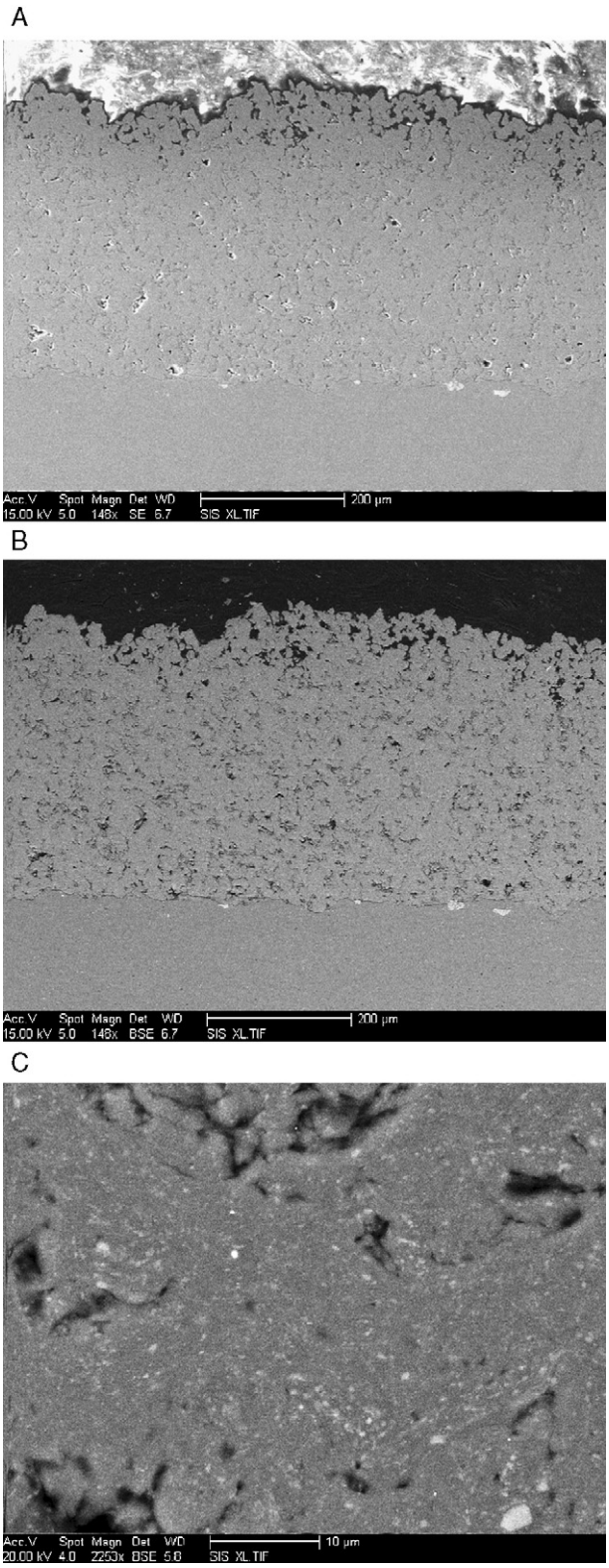

Fig. 4. Coatings produced by CGDS from as-cryomilled powder.

Table 3
Nanoindentation data (GPa)

As-atomized powder	As-cryomilled powder	Conventional coating	Nanocrystalline coating
2.32±0.2	4.19±0.2	3.75±0.3	4.41±0.5

although the morphology change induced by cryomilling seems to have resulted in a more evenly distributed histogram, suggesting a homogenization effect due to the non-spherical particle morphology. Again, this is observed only in the larger size range of cryomilled powder due to the enhancement of the drag of these particles by the increased drag coefficient and the projected surface area/particle volume ratio.

3.3. Coating microstructure

Fig. 3 shows the secondary (A) and backscattered (B and C) electron images of the coatings produced from the as-atomized powders. Fig. 3A demonstrates that limited porosity is present in the coating and that the interface between the coating and the substrate can barely be detected in secondary electron mode. In the backscattered electrons mode (Fig. 3B) the interface between the substrate and the coating is revealed and suggests a sufficient particle impact velocity during deposition that resulted in intimate bonding at the coating/substrate interface. Fig. 3C shows a detailed backscattered electron image of the as-atomized coating. It reveals the presence of Al_2CuMg intermetallics at the grain boundaries and Al_9FeNi precipitates distributed throughout the matrix. The same microstructure is observed in the atomized powder and it is described in detail elsewhere [26].

Fig. 3C also reveals two different deformation processes that occurred during impact, one is related to the deformation of the particle upon impact (splat behavior in solid state), and the other is a localized deformation process that is present at the particle boundaries (jet flow or adiabatic shear instability [27]). The first one is responsible for the mechanical locking of the constituent particles in the coating, while the second one occurs at the boundary of the particles and promotes an intimate metallic bonding between adjacent particles by breaking off the oxide layer that is naturally present in the feedstock aluminum powder. Nevertheless, both deformation processes are not directly linked and are not necessarily present in all the particles as shown in Fig. 3C where one can find undeformed particles with sheared microstructure at its boundaries and also flattened particles that experience adiabatic conditions during impact and show extensive plastic deformation in the interior of the particles.

Fig. 4 presents the SEM images of the nanocrystalline coatings, and due to its fine microstructure, the coating shows no microstructure details besides the dispersed Al_9FeNi submicron particles (Fig. 4C). While the cryomilled powder was sprayed under the same CGDS spray parameters that resulted in higher particle impact velocity both the coating/substrate and particle/particle boundaries are easily discernable and the porosity level is substantially higher (between 5%–10%) than in the conventional coating. This behavior is attributed to the fact that the cryomilled powder is much harder (Table 3) and difficult to deform, hence promoting the presence of porosity during deposition. Consequently, the increased velocity experienced by the cryomilled powder particles due to the enhanced drag force is insufficient to generate the required deformation level to produce as good a coating as the conventional powder produced. It is therefore concluded that cryomilled particles would need to reach higher impact velocities than conventional ones to achieve a coating with similar density.

The higher hardness and limited plastic deformation and flattening during impact are used to rationalize the lack of densification observed in the coating sprayed using the as-cryomilled powder. The improved particle velocities in the larger size range of cryomilled powder were not sufficient to compensate the high mechanical strength of the powder and promote extensive plastic deformation.

The nanoindentation results (500 nm in depth) for the powders and coatings, presented in Table 3, were used to quantify the hardness and explain the difference in coating density. The hardness of the nanocrystalline powder is substantially higher than that of the conventional one due to its finer microstructure (50 nm). Similarly, the hardness of the nanocrystalline coating [22] is higher than that of the conventional one. It can be observed that the hardness of the conventional coating is higher than that of the conventional powder, which suggests that the powder exhibited work hardening upon impact, increasing the density of dislocations within the grains and, therefore, the hardness of the coating. On the contrary, the hardness of the nanocrystalline coating is similar to that of the as-cryomilled powder, suggesting that there is no microstructural evidence of a heavily deformed grain structure in the cryomilled powder upon impact that can promote an increase in hardness (limited or no work hardening is observed).

4. Conclusions

Conventional and nanocrystalline 2618 Al alloy coatings were sprayed onto aluminum substrates using the Cold Gas Dynamic Spraying process. The conventional sprayed coating showed negligible porosity and an excellent interface with the substrate material as opposed to the nanocrystalline coating, in which the porosity level was in the range of 5 to 10%. The microstructure of the feedstock powders (atomized and cryomilled) was retained after the spray process.

The smaller particle size range exhibits a higher average particle velocity. This is attributed to the fact that the gas/particle momentum transfer or particle acceleration imparted by the gas is proportional to $1/d$, based on Newton's law and assuming a spherical particle, where d is the diameter of the particle to be accelerated. Consequently, higher acceleration and, therefore, particle impact velocity are to be expected when using a powder with a smaller particle size distribution. While both size ranges of cryomilled particles exhibit an increase in the drag force, this effect is more pronounced for the large size range. The combination drag coefficient/particle area–volume ratio acts favorably and contributes to the larger velocity increase of the larger cryomilled particles.

The difference in porosity between the conventional and nanocrystalline coatings can be explained by the hardness and microstructure of the corresponding feedstock powder: The softer and coarse-grain conventional powder experienced generalized adiabatic shear instability upon impact, resulting in a dense coating, whereas the harder and fine-grain cryomilled powder did not exhibit the same extent of deformation, resulting in porous coatings.

Acknowledgements

The authors wish to thank B. Cotter, J. MacDermid and L. Denner of the University of Ottawa Mechanical Engineering Department for their help with the Cold Spray system.

References

[1] A.P. Alkhimov, V.F. Kosarev, A.N. Papyrin, patent 5 302 414, 12/04/1994.
[2] D.L. Gilmore, R.C. Dykhuizen, R.A. Neiser, T.J. Roemer, M.F. Smith, J. Therm. Spray Technol. 8 (4) (December 1999) 576.
[3] R.C. Dykhuizen, M.F. Smith, J. Therm. Spray Technol. 7 (2) (June 1998) 205.
[4] R.C. Dykhuizen, M.F. Smith, D.L. Gilmore, R.A. Neiser, X. Jiang, S. Sampath, J. Therm. Spray Technol. 8 (4) (December 1999) 559.
[5] T. Schmidt, F. Gärtner et.al., Int.Th. Spray Conf. 2005 Proceedings, Basel, Switzerland, May 2005.
[6] C.C. Koch, Annu. Rev. Mater. Sci. 19 (1989) 121.
[7] E. Gaffet, N. Malhouroux, M. Abdellaoui, J. Alloys Compd. 194 (2) (May 1993) 339.
[8] F. Zhou, R. Luck, K. Lu, E.J. Lavernia, M. Ruhle, Philos. Mag., A, Phys. Condens. Matter, Struct. Defects Mech. Prop. 82 (5) (2002) 1003.
[9] C. Suryanarayana, Prog. Mater. Sci. 46 (1−2) (January 2001) 1.
[10] J. Eckert, J.C. Holzer, C.E. Kill III, W.L. Johnson, J. Mater. Res. 7 (7) (July 1992) 1751.
[11] D.B. Witkin, E.J. Lavernia, Prog. Mater. Sci. 51 (1) (January 2006) 1.
[12] M.J. Luton, C.S. Jayanth, M.M. Disko, S. Matras, J. Vallone, Mater. Res. Soc. Symp. Proc. 132 (1989) 79.
[13] B. Huang, J. Vallone, M.J. Luton, Nanostruct. Mater. 5 (4) (May 1995) 411.
[14] R.J. Perez, B. Huang, E.J. Lavernia, Nanostruct. Mater. 7 (5) (July 1995) 565.
[15] J.C. Rawers, Metall. Trans., A, Phys. Metall. Mater. Sci. 26A (3) (March 1995) 589.
[16] V.L. Tellkamp, S. Dallek, D. Cheng, E.J. Lavernia, J. Mater. Res. 16 (4) (April 2001) 938.
[17] L. Ajdelsztajn, B. Jodoin, G.E. Kim, J. Schoenung, Met. Mat. Trans. A 36 (3) (March 2005) 657.
[18] L. Ajdelsztajn, B. Jodoin, J. Schoenung, Surf. Coat. Technol. in press (Available online 28 February 2006).
[19] J. Majimel, G. Molénat, M.J. Casanove, D. Schuster, A. Denquin, G. Lapasset, Scr. Mater. 46 (2) (January 2002) 113.
[20] ASTM E11, Standard Specification for Wire Cloth and Sieves for Testing Purposes, Annual Book of ASTM Standards 14.02.
[21] X. Li, B. Bhushan, Mater. Charact. 48 (1) (February 2002) 11.
[22] L. Ajdelsztajn, A. Zúñiga, B. Jodoin, E.J. Lavernia, J. Therm. Spray Technol. 15 (2) (June 2006) 184.
[23] Tecnar automation DPV-2000 Reference manual.
[24] B. Jodoin, J. Therm. Spray Technol. 11 (4) (Decembre 2002) 496.
[25] P. Gerhart, R. Gross, J. Hochstein, Fundamentals of Fluid Mechanics, Addison−Wesley, 1985.
[26] L. Ajdelsztajn, A. Zúñiga, B. Jodoin, E.J. Lavernia, Surf. Coat. Technol. in press, Corrected Proof, Available online 19 July 2005.
[27] M. Grujicic, J.R. Saylor, D.E. Beasley, W.S. DeRosset, D. Helfritch, Appl. Surf. Sci. 219 (3−4) (December 2003) 211.